21 Swept Light Sources

Bart Johnson, Walid Atia, Mark Kuznetsov, Christopher Cook, Brian Goldberg, Bill Wells, Noble Larson, Eric McKenzie, Carlos Melendez, Ed Mallon, Seungbum Woo, Randal Murdza, Peter Whitney, and Dale Flanders

Keywords
Axsun Technologies • Coherence • Coherence revival • Mode locking • Ophthalmic imaging • Swept laser • Swept source

21.1 Introduction

In the early to mid-2000s, it became apparent that swept-source optical coherence tomography (SS-OCT) offers significant advantages over both time-domain (TD-OCT) and spectral-domain OCT (SD-OCT). Since that time, significant academic and commercial effort has been focused on developing SS-OCT lasers and sources capable of enabling high-quality SS-OCT imaging. While there are many important components in an SS-OCT system, it can reasonably be argued that the swept source is the most critical as its properties form the basis for most of the major system performance metrics. The detection and data acquisition electronics, together with the source, ultimately define the SS-OCT system performance specifications such as imaging speed, SNR and sensitivity, axial resolution, and imaging depth.

In this chapter, we describe a commercially available 1,060 nm swept-source OCT "engine" developed at Axsun Technologies suitable for ophthalmic and other OCT imaging applications. The engine consists of a swept laser module, control electronics, k-clock, balanced receiver, and data acquisition board which samples on k-clock transitions. The OCT engine provides optical system performance for shot-noise-limited imaging. The engine is designed to simplify construction of OCT imaging systems; the final user provides the optical probe/interface, application

B. Johnson (✉) • W. Atia • M. Kuznetsov • C. Cook • B. Goldberg • B. Wells • N. Larson • E. McKenzie • C. Melendez • E. Mallon • S. Woo • R. Murdza • P. Whitney • D. Flanders
Axsun Technologies, Billerica, MA, USA
e-mail: bjohnson@axsun.com

W. Drexler, J.G. Fujimoto (eds.), *Optical Coherence Tomography*,
DOI 10.1007/978-3-319-06419-2_22

control electronics, computing, and specialized software. Axsun manufactures such optoelectronic swept-source OCT engines for a range of medical imaging applications.

Axsun's 1,060 nm laser with 110 nm tuning range and 100 kHz sweep speed is described in this chapter along with the associated engine electronics. This is just one design point in the Axsun design space; many other swept source and engine configurations are possible and have been realized using the Axsun technology platform. For example, swept sources with various sweep rates, tuning ranges, coherence lengths, and modes of operation have been manufactured in both 1,060 and 1,310 nm wavelength ranges.

This chapter begins with a general description of the Axsun laser design along with a theoretical description of the laser dynamics. Next, we use this theory to explain a recently discovered property of the Axsun swept laser known as coherence revival [12]. We then describe the OCT engine electronics and demonstrate shot-noise-limited performance with sensitivities greater than 103 dB at 1.9 mW sample power. Lastly, we show artifact-free images from both internal testing and Topcon Corporation, a leading supplier of ophthalmic OCT imaging systems.

21.2 Laser Operation

In general, a swept laser consists of a gain medium, a tunable wavelength selection filter, and a laser cavity that supports lasing over the desired wavelength range. The Axsun laser architecture is shown in Fig. 21.1 and contains a reflective MEMS tunable Fabry-Perot filter, a broadband 1,060 nm gain chip, and a fiber reflector that forms the other end of the laser cavity and serves as the output coupler [1]. The filter exhibits a tunable reflection peak due to the filter optical axis tilt with respect to the optical beam [1, 2], and filter tuning is accomplished by changing the drive voltage on the MEMS filter. The MEMS filter can be swept from DC up to several hundred kilohertz depending on the desired repetition rate. The fiber extension brings the equivalent air length of the cavity to 104 mm such that there are a handful of laser cavity modes underneath the filter at all times. The laser is constructed in a hermetically sealed butterfly package with a fiber-optic feed through and exhibits stable polarization due to the strong TE/TM gain asymmetry of the SOA gain chip.

Many rapidly swept lasers exhibit a preference for tuning short to long wavelength [4–6]. They have higher power and are more stable in that direction. This behavior has been attributed to four-wave mixing in the gain medium [6, 7] coupled

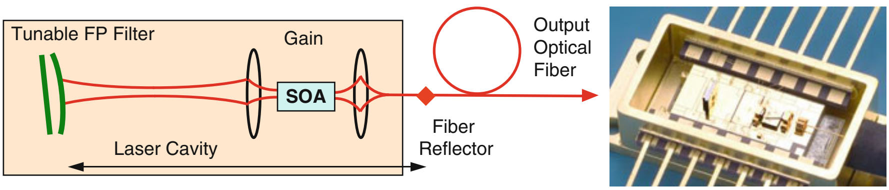

Fig. 21.1 External cavity laser with reflective Fabry-Perot MEMS tunable filter

with the Bogatov effect [8]. Computer simulations have predicted this red tuning behavior and laser pulsation under some conditions [7] and mode locking in some configurations [9]. We have shown both experimentally [3] and theoretically that sweeping the laser rapidly induces passive mode locking in the Axsun laser. Here we describe the basic dynamics of the laser.

Rapidly swept lasers tune too quickly for lasing to build up anew from spontaneous emission at each new wavelength [10]. A nonlinear optical mechanism is required to shift the wavelength of light circulating within the laser cavity to match the wavelength of the filter on successive round trips. In the case of the Axsun laser, a Doppler shift from the moving MEMS filter mirror does part of the job, although it is small compared to the wavelength shift required. Most of the shift comes from self-phase modulation induced by depletion of the gain as the mode-locked pulse travels through the semiconductor gain medium. Gain depletion is accompanied by a rise in refractive index. The coupling between the index and the power gain can be described using the linewidth enhancement factor, α, as

$$\Delta n = -\alpha \frac{\lambda}{4\pi} \Delta g$$

The mode-locking process is illustrated in Fig. 21.2. The SOA becomes optically longer as the pulse travels through, red shifting the light field. The laser does not tune continuously, but rather hops discretely to the next wavelength on each new pulse. The frequency hop for a SOA of length l is

$$\Delta v = -\frac{l}{\lambda} \frac{dn}{dt}$$

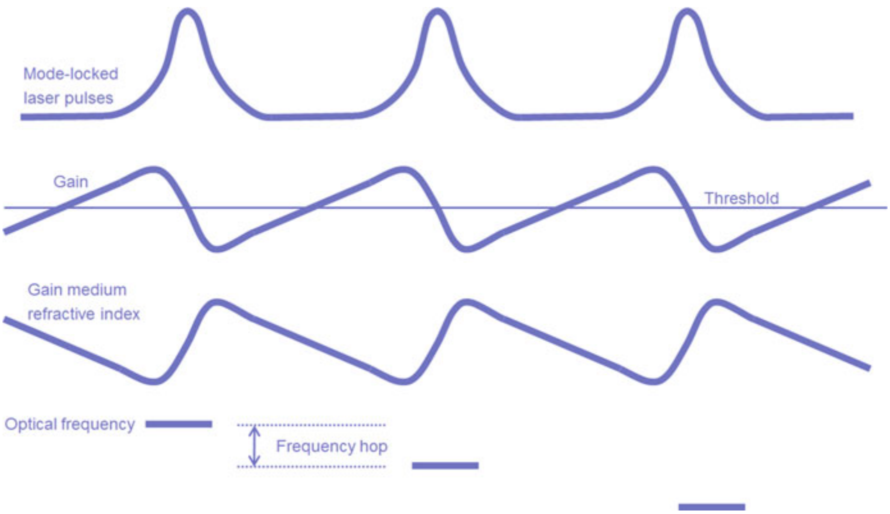

Fig. 21.2 Mode-locking and frequency hopping dynamics of a rapidly swept laser

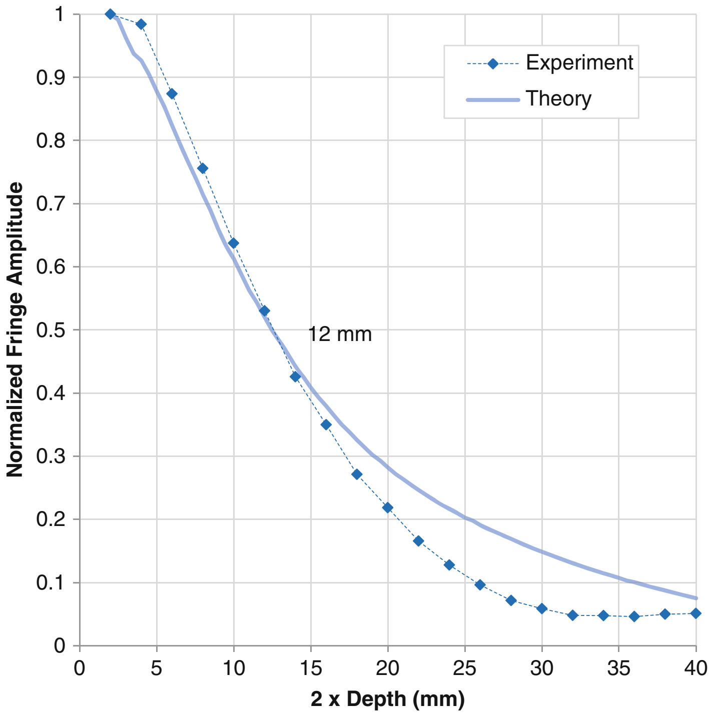

Fig. 21.3 Coherence length measurement compared with mode-locking model calculation

The pulse energy and width determine the magnitude of the frequency hop. The laser operates in this manner because the lowest threshold is obtained when the pulse frequency hops to follow the filter tuning. A feedback mechanism built into the laser dynamics naturally ensures the pulse hops to follow the filter. In the swept steady state, the pulses are tuned slightly to the long wavelength side of the filter and away from the reflection peak. If a pulse gets ahead of the filter (gets too red), it is attenuated by the filter and the lower power ensures the next pulse does not hop as far. Similarly, if a pulse falls behind (gets too blue), it becomes more powerful and catches up with the filter.

The filter line width and sweep rate play a critical role in ensuring proper mode-locking behavior throughout the sweep. The MEMS filter sweep is linearized to provide a nearly constant sweep rate during the tuning cycle. Stable passive mode-locking behavior can be maintained over the 100 nm data collection range of the laser with a total sweep range of 110 nm. This is essential for obtaining low relative intensity noise (RIN) and maintaining clean k-clocks for the optical engine.

We have developed a theory of these rapidly swept lasers, building on the mode-locking work by Haus [11]. This theory describes this mode-locking behavior in detail and can accurately predict a variety of laser characteristics, such as coherence lengths, as indicated in Fig. 21.3 below, and coherence revival properties, as discussed in the next section.

The upper limit of the coherence length of the mode-locked swept laser is determined by the pulse width. Theory predicts considerable chirp to the pulses, reducing the coherence lengths below this upper limit. The coherence length of these lasers is typically 12 mm, which ensures deep imaging capability required for many applications.

21.3 Coherence Revival

The 1,060 nm, 100 kHz laser operates with two pulses traveling in the cavity at once, with the two pulses separated by half the cavity roundtrip time. This can be seen with a high-speed detector and oscilloscope. Normally, an OCT interferometer is set up for short path mismatches, where laser pulses are interfering with themselves. With longer path mismatches, pulses can interfere with their neighbors, leading to the "coherence revival" phenomenon [12]. This behavior is shown in Fig. 21.4. The physical cavity length is 104 mm, but there is also interference at 52 mm due to the double pulsation. A pulse two away is an amplified copy of the first, whereas an adjacent pulse is not. There are two semi-independent pulse trains inside the cavity, leading to a 52 mm coherence function revival that is weaker than the revival at 104 mm.

Coherence revival is important because it can be a source of artifacts in an OCT system. An OCT interferometer needs to be carefully designed so that small stray reflections are not separated by intervals of half-cavity lengths, 52 mm, 104 mm, 156 mm . . . etc., where they can produce artifacts in the OCT image.

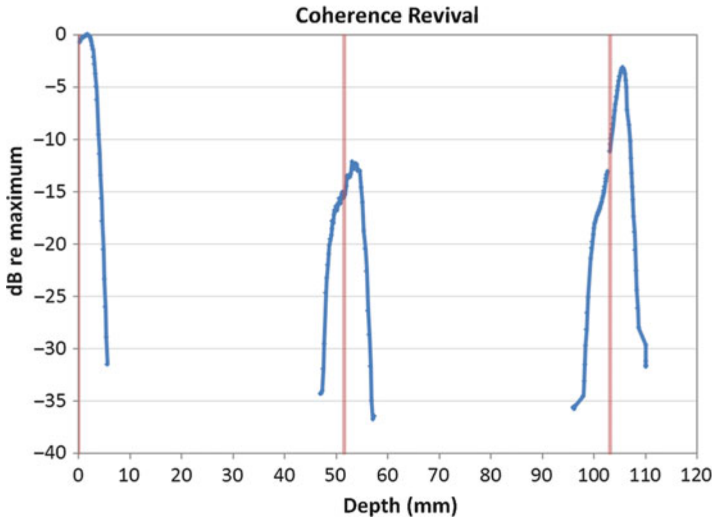

Fig. 21.4 Coherence function of the laser over a wide depth range showing the coherence revival phenomenon. The *red vertical lines* show the depths where the electrical signal frequency is zero. This measurement was made using an engine with a limited detector bandwidth, so the roll off of the curves reflects the detector bandwidth rather than the coherence length of the laser

Coherence revival has also been used to advantage to extend the imaging range of an OCT system [12]. Figure 21.4 shows that the 104 mm peak is displaced from the zero beat location. This means that the signal first goes up with depth before eventually rolling off. The imaging range, which normally is limited by the coherence length, is effectively doubled for this laser when operating at interferometer path mismatches near the 104 mm coherence revival peak. This coherence peak shift is a consequence of the pulse chirp and is a property of this particular laser design. By modifying the cavity design, it is possible to produce sources that do not have this behavior.

21.4 OCT Engine Design

The OCT engine consists of the swept laser module along with control electronics, a calibration k-clock, detection/receiver electronics, and a data acquisition board which samples on k-clock transitions. The engine is designed to simplify construction of OCT imaging systems; the end user provides the optical probe/interface, application control electronics, computing, and specialized software. Figure 21.5 shows a block diagram of the OCT engine.

The laser control board drives the SOA and MEMS tunable filter. The SOA current and filter drives are controlled through a file stored in flash memory. The control file specifies the SOA current and filter voltages as a function of time. In addition, the board contains two optical receivers. The first is for the calibration k-clock. The k-clock serves as an external clock input to the data acquisition (DAQ) board analog to digital (A2D) converter. A balanced receiver detects light from the main OCT imaging interferometer. The balanced receiver output, k-clock, and sweep trigger are differential signals for noise immunity and are run between the boards over SATA cables commonly used for disk drive interfaces.

In swept-source OCT, it is necessary to translate the raw OCT signal from one that is evenly spaced in time to one with data points evenly spaced in optical frequency, or k. This is often done through various software resampling approaches that interpolate the raw OCT signal. The resampling coefficients can be derived at predetermined intervals or on every A-line, depending on the stability of the swept source and the required imaging accuracy. Either way, the raw OCT signal must be resampled during each A-line.

An alternative approach, and the one used in the Axsun OCT engine, is to use a digital k-clock [13, 16]. The k-clock is derived from a fiber-based Mach-Zehnder interferometer (MZI) as shown in Fig. 21.5. As the laser source sweeps across its wavelength tuning range, the MZI receiver has zero-crossings that are evenly spaced in optical frequency. The MZI path length difference must be four times the maximum imaging depth (interference length $= 2 \times$ depth) in order to satisfy the Nyquist sampling limit. This approach speeds up data acquisition by eliminating the computing time for external resampling. However, this approach requires the A2D converter to handle a wide range of k-clock frequencies and duty cycles due to the nonlinear sweep dynamics of the laser.

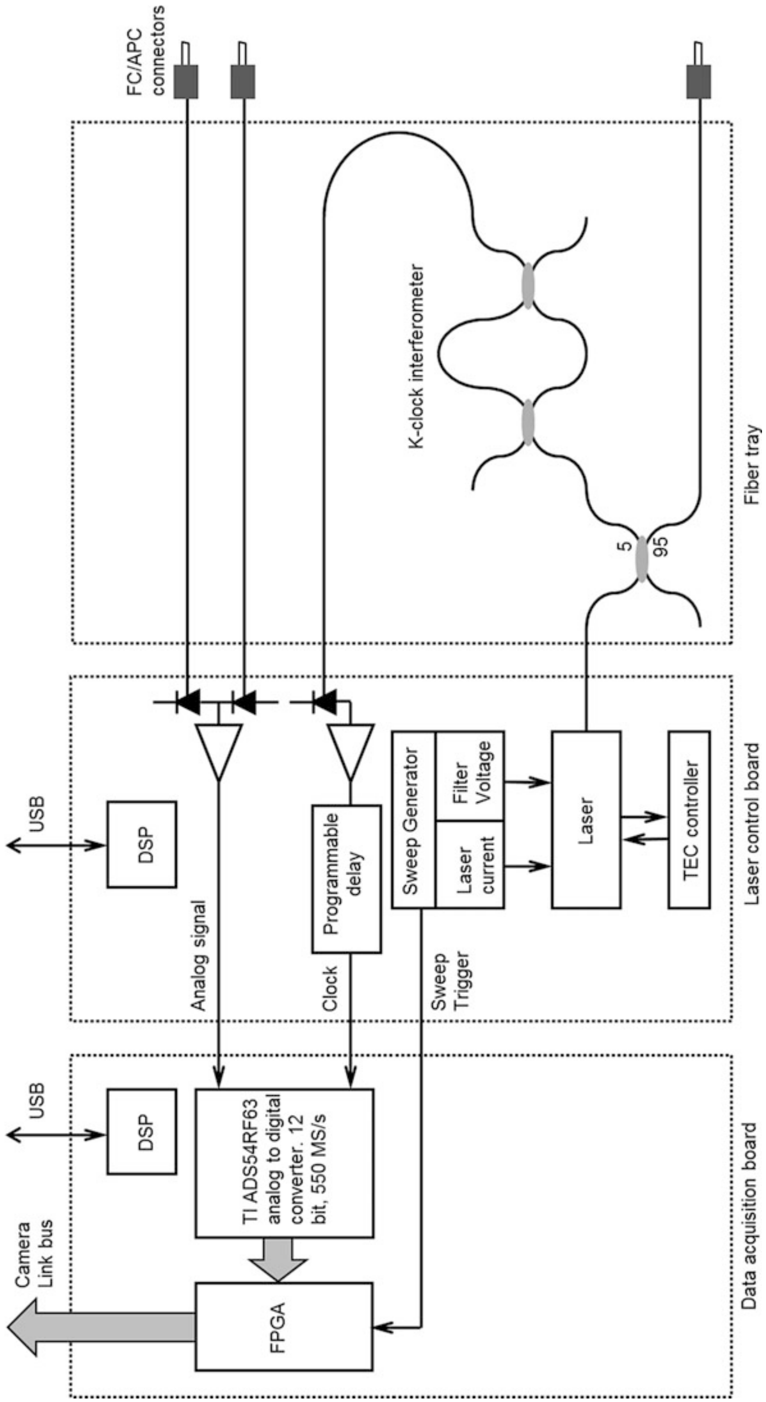

Fig. 21.5 Block diagram of the Axsun OCT engine

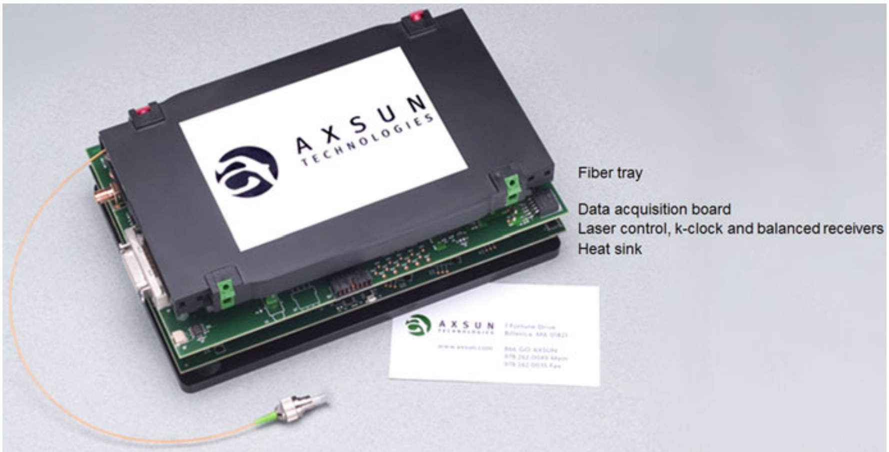

Fig. 21.6 Physical construction of the Axsun OCT engine

The data acquisition card in the Axsun OCT engine utilizes a 12-bit Texas Instruments ADS54RF63 analog to digital (A2D) converter. This chip is very tolerant of varying clock frequencies and duty cycles. Its clock specification is 40–550 MHz. We have verified that the DAQ card performs up to the limits of the chip. The FPGA presents the glue logic between the A2D converter and the Camera Link bus. The Camera Link bus can be set to run at 83.3, 41.7, 20.8, or 10.4 MHz. Two 12-bit samples are issued per clock cycle. There is no on-board data storage, but there is an FIFO buffer that mediates between the incoming variable data rate samples and the fixed rate Camera Link output samples. The engine must fill the FIFO faster than it is emptied and must not issue more samples than can be transferred between sweep trigger pulses. The system described in this chapter runs the Camera Link bus at 83.3 MHz. The laser is swept to keep the k-clock frequency greater than 167 MHz, so the FIFO is never empty. At the 100 kHz sweep rate, it transfers 1,376 out of a maximum of 1,670 samples.

The fiber Mach-Zehnder k-clock interferometer is located in the fiber tray. It is precisely cut and fusion spliced to set the maximum depth (Nyquist fold over distance) to an accuracy of ± 100 µm. Figure 21.6 shows a picture of the OCT engine stack.

Both laser control and DAQ boards can communicate with a personal computer via USB interfaces. A control program, OCTHost, is provided, but customer software can utilize a Windows .NET assembly for custom control.

21.5 System Performance

The Axsun OCT engine described in this chapter is set up for the scan plan in Fig. 21.7. The maximum imaging depth, set by the k-clock interferometer mismatch, is 3.7 mm. The laser sweeps over 110 nm at 100 kHz sweep rate. One thousand three hundred and seventy-six (1,376) samples are acquired, which

Parameter	Min	Value	Max	Units
Maximum scan depth in air		3.7		mm
FSR of clock interferometer		20.26		GHz
Sweep Frequency		100		kHz
Wavelength Range	985.0		1095.0	nm
Optical Frequency Range	273.783		304.358	THz
Data Range in wavelength	989.4		1089.6	nm
Data Range in optical frequency	275.144		302.997	THz
Sweep Range		110.0		nm
Sampled Range		100.2		nm
Maximum possible samples		1509		
Percent bandwidth used		91		%
Selected number of samples		1376		
Pixels in A-scan		688		
Data collection duty cycle		44		%
Estimated Clock Frequency		313		MHz

Window type	Resolution			
	3 dB	10 dB	20dB	Units
Cosine	6.4	11.0	14.6	µm
Hamming	7.0	12.4	16.6	µm
Hann	7.8	13.6	17.8	µm
Dolph-Chebyshev 60 dB	7.8	13.8	18.7	µm
Blackman	8.9	15.7	21.4	µm
Dolph-Chebyshev 80 dB	8.9	15.9	21.8	µm
Dolph-Chebyshev 100 dB	9.9	17.8	24.5	µm

Fig. 21.7 Scan plan for the 1,060 nm OCT engine. *Yellow* cells are inputs to the calculation. The Hann window is used in all of the measurements and calculations presented here

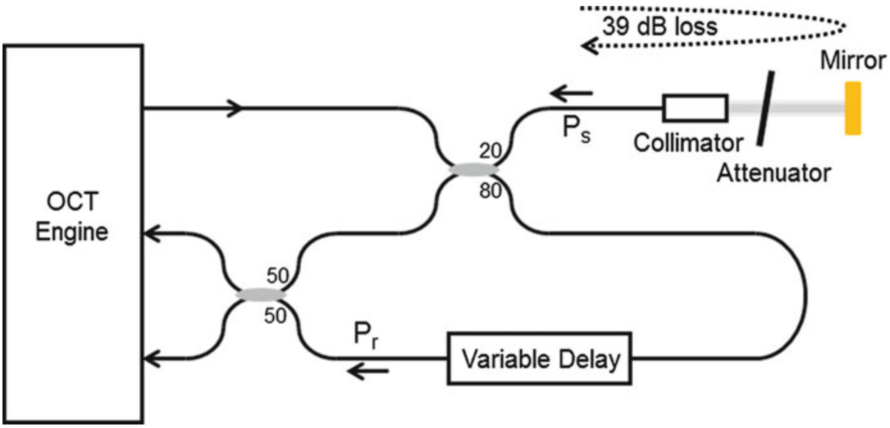

Fig. 21.8 Test interferometer

represents 100 nm of data out of the 110 nm sweep. Although the laser power output is not flat across the sweep, imaging depth resolutions very close to the limits imposed by the pre-FFT window function are obtained. All of the data presented here use a Hann window, though other windows can be chosen to trade resolution for side mode suppression. Calculated theoretical resolutions at 3, 10, and 20 dB from the point spread function peak are listed in the table.

System average output powers exceed 15 mW. The laser control board blanks the laser output power over the nonfunctional retrace portion of the laser frequency sweep. Given the roughly 50 % on/off duty cycle, the imaging power is roughly twice the average. This ensures high SNR while limiting average optical power, which is important, for example, in ophthalmic applications that have strict limits on the average optical power exposure to the eye.

Much of the OCT engine performance testing has been done with an interferometer configured as shown in Fig. 21.8. For imaging experiments, the attenuator and mirror are replaced by a galvo-scanner and imaging lens. Production systems are all tested in an automated test setup for sensitivity, resolution, imaging artifacts, and overall functionality. Most of the data presented here uses the setup of Fig. 21.8.

A calibration table defines the swept laser current and MEMS filter tuning voltage versus time. Each laser frequency sweep is calibrated separately, and a clock analysis similar to that in Fig. 21.9 verifies the calibration. At 100 kHz repetition rate, the filter is being driven well beyond its mechanical resonance, which limits the data collection duty cycle to around 45 % due to the resulting limitations in the linearization of the filter sweep. The red portion of the curves delimits the data collection region which proceeds for 1,376 clock pulses following the trigger. Power is measured with a wide bandwidth photodetector and a 2.5 GHz bandwidth oscilloscope. This is fast enough to see the mode-locked pulses. The wide bandwidth power trace is shown along with a 5 MHz low-pass filtered trace in red. The instantaneous powers are calibrated from an average power measurement made with a power meter.

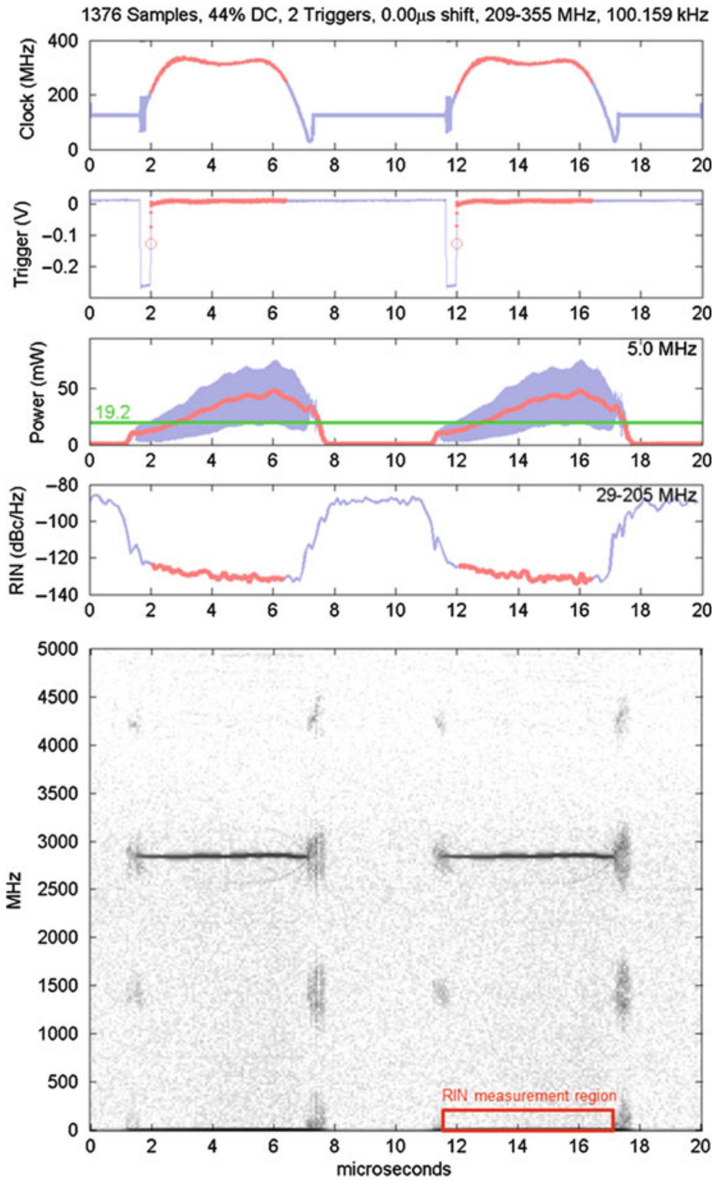

Fig. 21.9 Clock analysis, power, RIN, trigger, spectrogram

An RIN estimate is made from the wide bandwidth power data. It is based on the average noise between 29 and 209 MHz, which is approximately the bandwidth of the balanced receiver. Due to the laser pulsations, there are large RF signals outside this frequency range, but only the signals within the balanced receiver bandwidth are relevant. This high-speed measurement is routinely done to look for laser

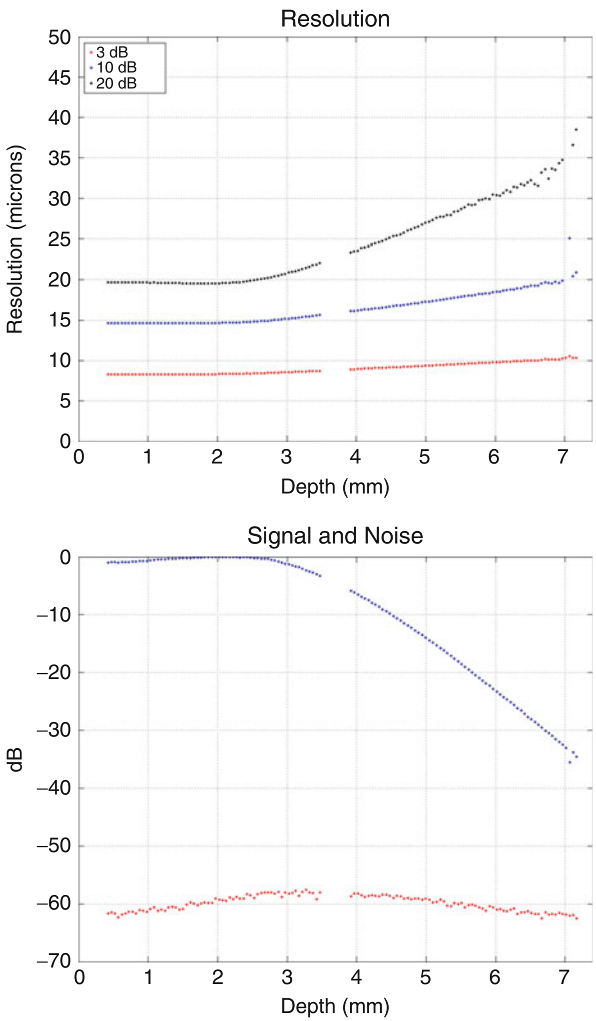

Fig. 21.10 Measured imaging depth resolution at 3, 10, and 20 dB below the point spread function peak. A Hann window was used in processing the data. Conditions: 1.2 mW reference power, 1.9 mW sample power, 46 dB loss. Signal and noise variations with depth are shown in the lower plot

instabilities. However, the RIN is too low to measure accurately by this method and only a rough estimate is obtained. In fact, high-performance telecommunication RIN test sets subtract out receiver noise and calculated shot noise when doing this type of test. Better RIN estimates can be obtained through measurements of system SNR as a function of reference power.

The bottom plot of Fig. 21.9 is a spectrogram of the wide bandwidth detector signal. It shows a strong signal at 2.9 GHz, indicating that the laser is pulsing twice per round trip in a 104 mm cavity. The clean spectrum between DC and 200 MHz indicates low RIN. The time-resolved nature of the spectrogram can reveal local laser instabilities where the laser is not cleanly mode locked.

Resolution and roll off measurements made on our automated test station are shown in Fig. 21.10. Resolution measurements generally match well to the

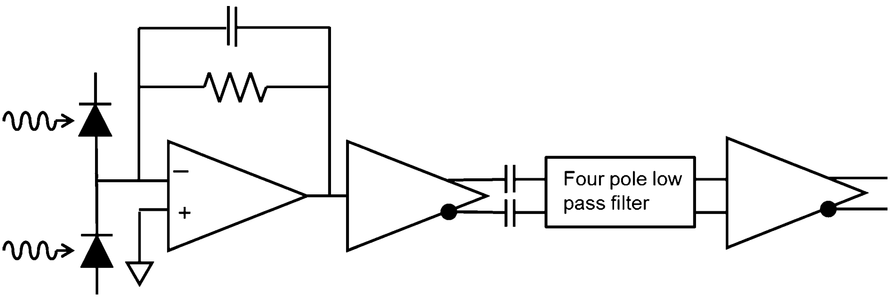

Fig. 21.11 Design of balanced receiver

calculations in the table of Fig. 21.7. These measurements were made through the depth range of 3.7 mm, and the aliased peaks beyond 3.7 mm were also tracked. Second- and third-order numeric dispersion compensation was used [14] and the sign of the compensation was flipped once the 3.7 mm Nyquist point was passed. An error in dispersion compensation broadens the point spread at all depths. It is also important to have the clock and balanced receiver signal time synchronized [15, 16]; otherwise, the resolution degrades with depth. System fiber lengths must be cut properly to achieve this. A programmable clock delay on the laser control board (see Fig. 21.5) can also be used to fine-tune the delay to minimize this effect.

Tracking roll off data past the 3.7 mm Nyquist depth shows the effectiveness of the antialiasing filters, which are located on the balanced receiver and the DAQ boards. The noise plotted is the noise level at the signal depth. It is nearly flat, as expected from shot-noise-limited operation. The test station uses a 1.2 mW reference power for these measurements.

The balanced receiver shown in Fig. 21.11 is a two-stage design followed by a differential output stage that drives the SATA cable connection to the data acquisition board. It has a transimpedance of 16 kohms and a frequency response shown in Fig. 21.12. It is AC coupled with a four-pole low-pass filter for antialiasing. It is thermal-noise limited at low frequency, but the noise is peaked at higher frequencies due to the operational amplifier input noise multiplied by the noise gain of the circuit [17]. This is an expected behavior for this type of receiver and means that the receiver noise is not flat versus depth.

The data acquisition system is another source of noise. The Axsun Camera Link DAQ card utilizes a Texas Instruments ADS54RF63 analog to digital converter. It is a 12 bit pipelined converter rated for a 40–550 MHz clock range. Axsun's own noise measurements with the card are shown in Fig. 21.13. The card is able to meet the ADS54RF63 noise specifications over the rated frequency range, but can also be under- or over-clocked with reduced performance. The converter translates ± 1.1 V differential signals into a 12 bit offset binary code. It achieves $\sigma = 0.9$ count RMS noise over much of its range. That translates to a maximum SNR of 64 dB and an ENOB of 10.4 bits, given the following expressions [18]:

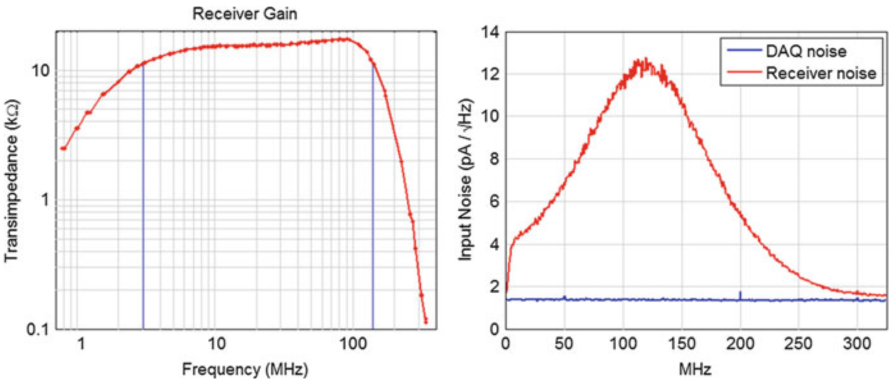

Fig. 21.12 Frequency response data for the balanced receiver. Transimpedance (*left*) and effective input current noise (*right*) are plotted

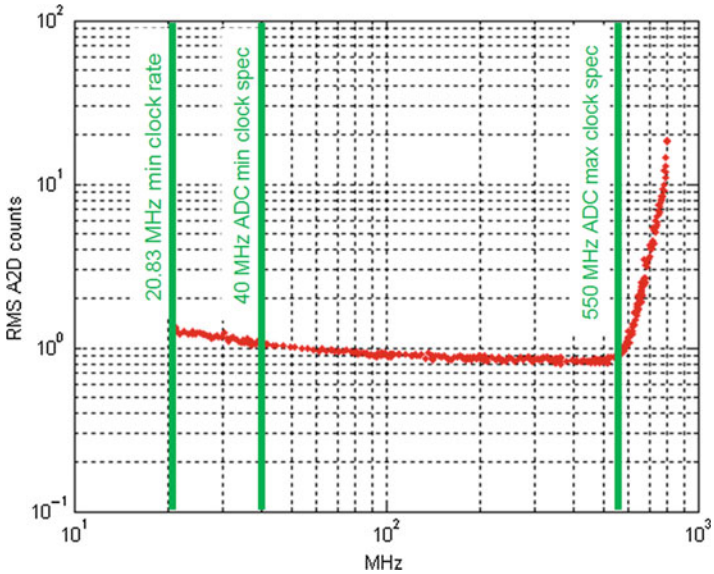

Fig. 21.13 Noise floor of data acquisition board

$$\mathrm{SNR} = \frac{\left(2^{N_{\mathrm{bits}}-1}\right)^2}{2\sigma^2}$$

$$\mathrm{SNR} = 6.02 \cdot \mathrm{ENOB} + 1.76\ \mathrm{dB}$$

Note that the 64 dB converter SNR limit is a broadband limit. FFT processing, which narrows the bandwidth, effectively averages OCT signals to much higher signal-to-noise ratios.

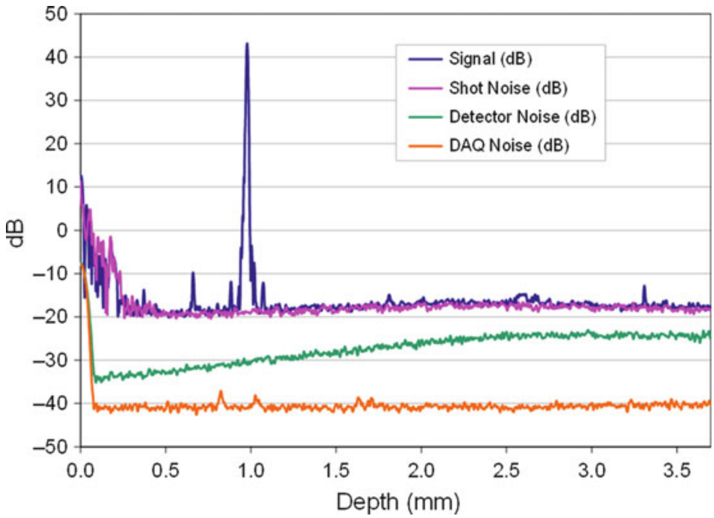

Fig. 21.14 Plot of signal and noise floor components versus depth. Conditions: 2.0 mW reference, 1.8 mW sample power, 39 dB attenuation

Figure 21.14 shows system noises versus depth along with the signal for a fixed reflector at 1 mm depth. It shows that the shot noise limit can be achieved throughout the imaging depth range. The traces are averages of 100 sweeps. Since the phase information is thrown away before averaging, the SNR is the same as for a single sweep, but the hash in the noise floor is reduced to give a better noise estimate. DAQ noise is not a limiting factor because the receiver noise is higher. The receiver noise is also not a limiting factor because the shot noise with 2 mW reference power is much higher. The shot noise is also flat because the transimpedance of the amplifier is flat up to the Nyquist frequency. The receiver noise is not flat, as pointed out earlier, because the noise gain of the receiver circuit is not flat. The useable depth range in this case is about 0.3–3.7 mm.

Figure 21.15 shows how the signal and noise behave as a function of reference power. Around 100 μW the shot noise becomes higher than the receiver noise. At this point the SNR becomes shot noise limited. Note that the SNR does not fall with further increases in reference power as expected from RIN-limited operation. The laser has very low noise. The data shown is limited to 2 mW, as measured on a power meter, which is getting close to the saturation limit of the balanced receiver.

The OCT engine's signal-to-noise behavior is modeled by the following expression, which is similar to that in reference [19]. Reference and sample powers, P_r and P_s, are defined in Fig. 21.8. The digital processing loss is 1.8 dB for a Hann window [20]. We estimate 2.2 dB miscellaneous loss:

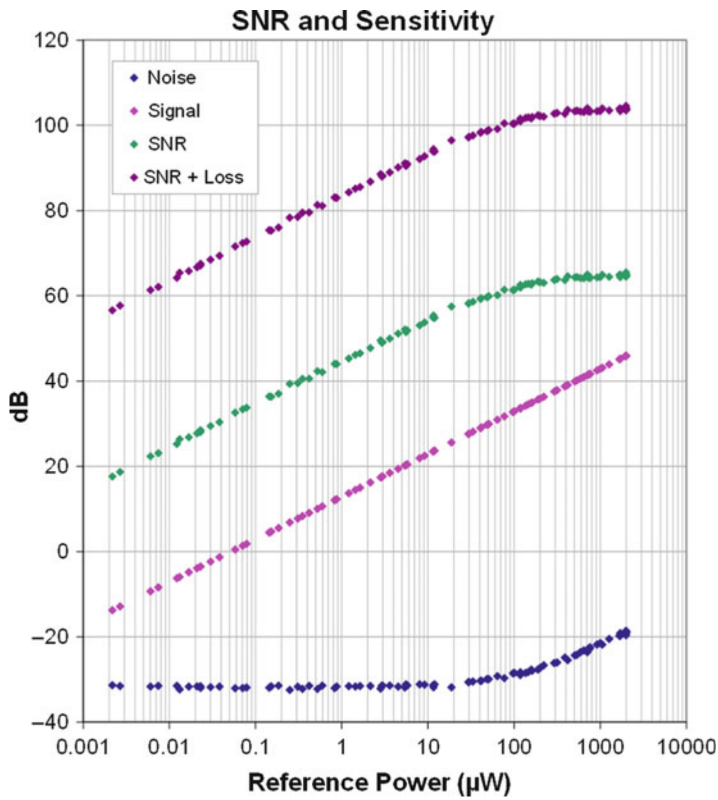

Fig. 21.15 Signal, noise, SNR, sensitivity versus reference power at 1 mm depth and 39 dB loss

$$\mathrm{SNR} = \frac{2\dfrac{T_{\mathrm{Misc}}T_{\mathrm{Coupler}}}{L_{\mathrm{Proc}}}\left(\dfrac{\eta q}{hv}\right)^2 P_r P_s}{\left[\left(\dfrac{\eta q}{hv}\right)^2 \mathrm{NEP}^2 + 2\dfrac{\eta q^2}{hv}P_r + \left(\dfrac{\eta q}{hv}\right)^2 \mathrm{RIN}\cdot\mathrm{CMRR}\cdot P_r^2\right]\dfrac{2B}{N}},$$

where

P_r = reference beam power
P_s = sample beam power
η = detector quantum efficiency
q = electronic charge
L_{Proc} = digital processing loss
T_{Coupler} = optical coupler power transmission
T_{Misc} = miscellaneous transmission reductions, such as connector and coupler loss

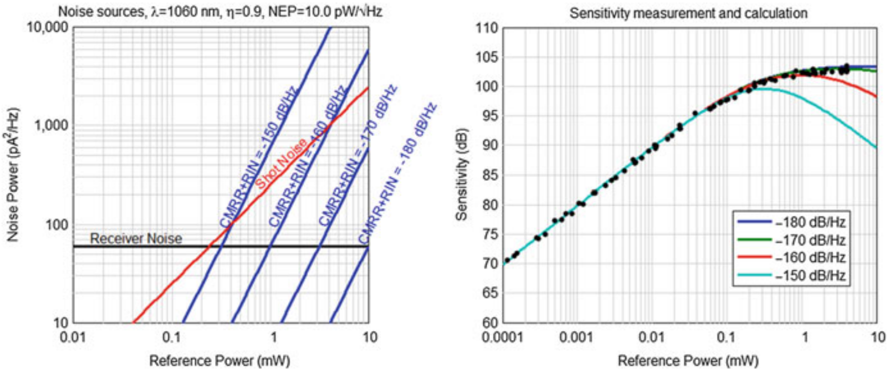

Fig. 21.16 Calculated noise powers (*left*) and comparison of experimental and theoretical sensitivities (*right*)

$h\nu$ = photon energy
NEP = noise equivalent power of receiver
RIN = relative intensity noise
CMRR = common mode rejection ratio of balanced receiver
B = bandwidth of optical receiver (assumed 1/2 sampling rate)
N = number of samples

As pointed out in the discussion of the RIN measurement in Fig. 21.9, we believe that those numbers are pessimistic for the reasons illustrated in Fig. 21.16. We cannot determine the RIN directly from a measurement of SNR versus reference power, but we can get an estimate of CMRR+RIN (in dB/Hz). The left plot shows the noise floors for several values of CMRR+RIN. For shot noise to dominate, the RIN must be very low, because the CMRR will be poor given that the splitting ratios of fused 1,060 nm 3 dB couplers are not accurate and vary over wavelength. The right-hand plot of Fig. 21.16 shows no decrease in SNR at high reference power. It is likely that CMRR+RIN < -170 dB/Hz. We have not measured our CMRR, but it is probably around 20 dB. That would put the laser RIN in the neighborhood of -150 dB/Hz, much better than we can measure using the methods of Fig. 21.9. The laser has very low noise.

21.6 Images

The OCT engine described above, when coupled with a well-designed imaging interferometer and sample arm probe, is capable of delivering high-speed, high-resolution, high-sensitivity OCT images. The interferometer of Fig. 21.8 is well suited to ophthalmological applications where the average power to the eye is limited. An example image is shown in Fig. 21.17.

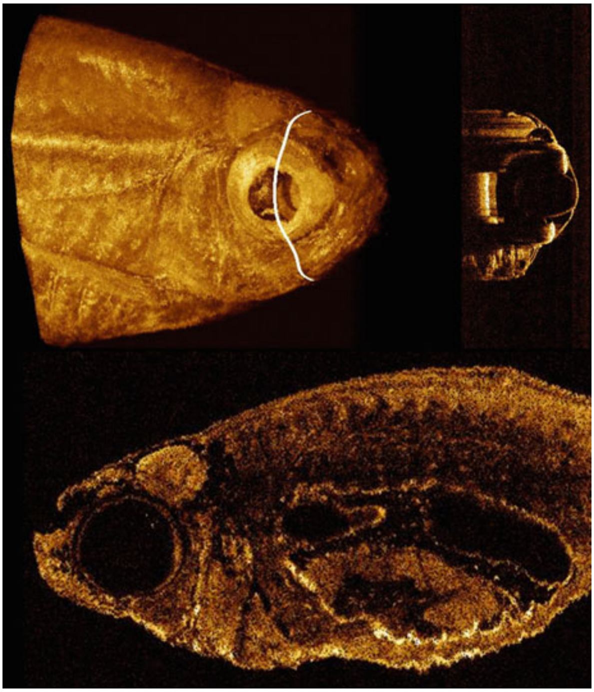

Fig. 21.17 Small aquarium fish imaged in the Axsun Technologies laboratories

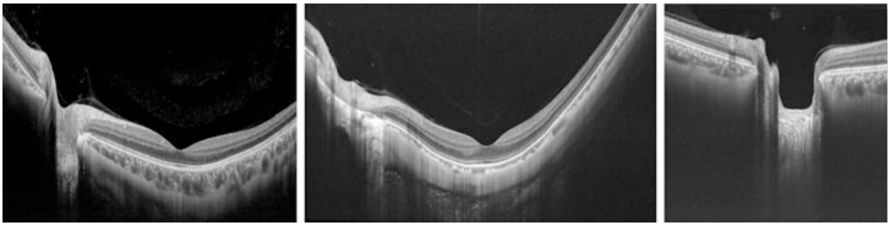

Fig. 21.18 Topcon DRI OCT-1 Atlantis system images of a healthy retina (*left*), a high myopia patient (*center*), and the optic nerve head (*right*) (Images courtesy of Topcon Corporation and Kyoto University)

High-quality retinal images in commercial equipment using the Axsun 1,060 nm OCT engine have also been produced. Figure 21.18 shows retinal images from a Topcon DRI OCT-1 Atlantis system. The 1,060 nm wavelength has several advantages over the current generation of 850 nm imaging systems. Reduced light scattering at longer wavelengths means that 1,060 nm light can penetrate deep into the choroid layer behind the retina. This wavelength also has superior penetration through cataracts. Another advantage is that the light is invisible to the patient, reducing eye motion from the patent's eyes natural tendency to follow the beam. The Axsun OCT engine also sweeps faster than current generation ophthalmic OCT systems and has shot-noise-limited performance, no fixed patterns, and low levels of ghost images.

21.7 Summary

In this chapter we described the design and performance of a 1,060 nm swept laser OCT imaging engine. In addition, we presented a new description of the passive mode-locking behavior of the Axsun swept laser. This deeper understanding of the swept laser dynamics is an important tool for many reasons. It enables modeling and rapid development of new lasers to meet the evolving needs of the OCT academic and commercial communities. In addition, the model allows us to better understand the design tolerance to changes in various key components, which is important for manufacturing these products with low cost.

The laser module, surrounding control and data acquisition electronics, produces an OCT engine that can accelerate commercial OCT system development. An OCT system manufacturer can concentrate on the application, the optical interface and software control. Axsun can provide high-speed shot-noise-limited system performance. This chapter shows one particular engine design useful for medical imaging, but Axsun has the ability to address other imaging and measurement problems with modifications to these systems. In particular, Axsun has both 1,310 and 1,060 nm band swept sources. They can be provided in a variety of sweep speeds, coherence lengths, and modes of operation.

References

1. M. Kuznetsov, W. Atia, B. Johnson, D. Flanders, Compact ultrafast reflective Fabry-Perot tunable lasers for OCT imaging applications. Proc. SPIE **7554**, 75541F-1 (2010)
2. D.C. Flanders, M.E. Kuznetsov, W.A. Atia, Laser with tilted multi spatial mode resonator tuning element, US Patent 7,415,049, issued 19 Aug 2008
3. B.C. Johnson, D.C. Flanders, Actively mode locked laser swept source for OCT medical imaging, US Patent application, Publication number US 2012/0162662 A1, 28 June 2012
4. S.H. Yun, B.E. Bouma, in *Optical Coherence Tomography*, ed. by W. Drexler, J.G. Fujimoto. Wavelength Swept Lasers, (Springer, ISBM 978-540-77549-2.), pp. 359–378
5. S.H. Yun, C. Boudoux, M.C. Pierce, J.F. de Boer, G.J. Tearney, B.E. Bouma, Extended-cavity semiconductor wavelength-swept laser for biomedical imaging. IEEE Photon. Technol. Lett. **16**, 293–295 (2004)
6. S.H. Yun, C. Boudoux, G.J. Tearney, B.E. Bouma, High-speed wavelength-swept semiconductor laser with a polygon-scanner-based wavelength filter. Opt. Lett. **28**, 1981–1983 (2003)
7. A. Bilenca, S.H. Yun, G.J. Tearney, and B.E. Bouma, Numerical study of wavelength-swept semiconductor ring lasers: the role of refractive-index nonlinearities in semiconductor optical amplifiers and implications for biomedical imaging applications, Opt. Lett. **31**, 760–762 (2006)
8. P. Bogatov, P.G. Eliseev, B.N. Sverdlov, Anomalous interaction of spectral modes in a semiconductor laser. IEEE J. Quantum Electron. **11**, 510–515 (1975)
9. E.A. Avrutin, L. Zhang, Dynamics of Semiconductor Lasers under Fast Intracavity Frequency Sweeping. 14th Int. Conf. on Transparent Optical Networks (ICTON), 1–4 (2012)
10. R. Huber, M. Wojtkowski, K. Taira, J.G. Fujimoto, Amplified, frequency swept lasers for frequency domain reflectometry and OCT imaging: design and scaling principles, Opt. Express **13**, 3513–3528 (2005)

11. H.A. Haus, Mode-Locking of Lasers, *IEEE Journal on Selected Topics in Quantum Electronics*, **6**, 1173–1185 (2000)
12. A. Dhalla, D. Nankivil, and J.A. Izatt, Complex conjugate resolved heterodyne swept source optical coherence tomography using coherence revival, Biomed. Opt. Express **3**, 633–649 (2012)
13. M.A. Choma, K. Hsu, J.A. Izatt, Swept source optical coherence tomography using an all-fiber 1300-nm ring laser source, J. Biomed. Opt. **10**, 044009 (2005)
14. M. Wojtkowski, V.J. Srinivasan, T.H. Ko, J.G. Fujimoto, A. Kowalczyk, J.S. Duker, Ultrahigh-resolution high-speed Fourier-domain optical coherence tomography and methods for dispersion compensation. Opt. Express **12**, 2404–2422 (2004)
15. E.D. Moore, R.R. McLeod, Correction of sampling errors due to laser tuning rate fluctuations in swept-wavelength interferometry, Opt. Express **16**, 13139–13149 (2008)
16. J. Xi, L. Huo, J. Li, X. Li, Generic real-time uniform K-space sampling method for high-speed swept-Source optical coherence tomography, Opt. Express **18**, 9511–9517 (2010)
17. J. Graeme, *Photodiode Amplifiers: Op Amp Solutions*, Chapter 5 – “Noise”, McGraw Hill, ISBN 0-07-024247-X
18. W. Kester, Taking the Mystery out of the Infamous Formula, ‘SNR = 6.02N + 1.76dB,’ and Why You Should Care, Analog Devices MT-001 tutorial
19. S.H. Yun, G.J. Tearney, J.F. de Boer, N. Iftimia, B.E. Bouma, High-speed optical frequency-domain imaging, Opt. Express **11**, 2953–2963 (2003)
20. F. Harris, On the use of windows for harmonic analysis with the discrete Fourier transform. Proceedings of the IEEE **66**, 51–83 (1978)